Biogeosciences
Discussions

Impact of North Brazil Current rings on air-sea CO₂ flux variability in winter 2020

Léa Olivier[1], Jacqueline Boutin[1], Gilles Reverdin[1], Nathalie Lefèvre[1], Peter Landschützer[2], Sabrina Speich[3], Johannes Karstensen[4], Markus Ritschel[2] and Rik Wanninkhof[5]

5 [1] LOCEAN-IPSL, Sorbonne Université-CNRS-IRD-MNHN, Paris, France
[2] Max Planck Institute for Meteorology, Hamburg, Germany
[3] Laboratoire de Météorologie Dynamique, ENS-Ecole Polytechnique-CNRS-Sorbonne Université, Paris, France
[4] GEOMAR Helmholtz Centre for Ocean Research, Kiel, Germany
[5] Atlantic Oceanographic & Meteorological Laboratory of NOAA, Miami, USA

10

Correspondence to: Léa Olivier (lea.olivier@locean.ipsl.fr)

Abstract. The North Brazil Current (NBC) flows northward across the Equator, passes the mouth of the Amazon River, and forms large oceanic eddies near 8°N. We investigate the processes driving the variability of air-sea CO₂ fluxes at different

15 scales in early 2020 in the region [50°W-59°W – 5°N-16°N]. This region is a pathway between the equatorial and North Atlantic Ocean and was surveyed during the EUREC⁴A-OA/ATOMIC campaign. In-situ surface fugacity of CO₂ (fCO₂), salinity and temperature combined with maps of satellite salinity, chlorophyll-a and temperature highlight contrasting properties in the region. In February 2020, the area is a CO₂ sink (-1.7 TgC.month⁻¹), previously underestimated by a factor 10. The NBC rings transport saline and high fCO₂ water indicative of their equatorial origins and are a small source of CO₂ at

20 regional scale. Their main impact on the variability of biogeochemical parameters is through the filaments they entrain into the open ocean. During the campaign, a nutrient rich freshwater plume from the Amazon River is entrained from the shelf up to 12°N and caused a phytoplankton bloom leading to a significant carbon drawdown (~20 % of the total sink). On the other hand, saltier filaments of shelf water rich in detrital material act as strong local sources of CO₂. Spatial distribution of fCO₂ is therefore strongly influenced by ocean dynamics south of 12°N. The less variable North Atlantic subtropical water extends

25 from Barbados northward. They represent ~60 % of the total sink due to their lower temperature associated with winter cooling and strong winds.

1 Introduction

The North Brazil Current is one of the dominant features of the tropical Atlantic circulation. In a region dominated by zonal

30 jets, it flows northward along the coast of South America and separates from the coast around 6-8°N. It seasonally retroflects to feed the North Equatorial Counter Current and thus close the equatorial wind-driven gyre. This retroflection occasionally

pinches off some of the world's largest eddies, the North Brazil Current rings (NBC rings, Johns et al., 1990; Richardson et al., 1994).

35   After their separation from the NBC retroflection region, the rings travel north-westward toward the Caribbean in a course parallel to the coast of South America. These eddies have been extensively studied using modelling and both, in-situ (e.g. 1998-2001 NBC Ring experiment, Wilson et al., 2002) and satellite observations. They have a mean radius of 200 km and their diameter can exceed 450 km. Vertically, some of them extend down to more than 1000 m (Fratantoni & Glickson, 2002; Fratantoni & Richardson, 2006; Johns et al., 2003). Different family of rings exists, and most of the anticyclonic eddies

40   detectable by altimetry are rather shallow, extending from the surface to 200-300 m (Garraffo et al., 2003; Wilson et al., 2002). They swirl clockwise and travel with an average north-westward translation speed of 8-15 km d^{-1} (Johns et al., 1990; Mélice & Arnault, 2017). When they reach the Lesser Antilles, they start to coalesce and disintegrate, partly due to interactions with the topography (Fratantoni & Richardson, 2006; Jochumsen et al., 2010). There is substantial variability in the number of rings shed per year, ranging from 5 (Aroucha et al., 2020; Fratantoni & Glickson, 2002; Mélice & Arnault, 2017, Goni & Johns,

45   2001) to 9 (Johns et al., 2003). NBC rings play a crucial role in the interhemispheric transport of salt and heat in the Atlantic Ocean and are an important part of the meridional overturning circulation (Johns et al., 2003). The NBC rings disrupt an already complex region located in the vicinity of the Amazon River mouth and at the transition between equatorial and subtropical waters.

50   While most of the studies on rings focused on their physical properties, little is known about their biogeochemical properties and how they affect the air-sea CO_2 flux of the western tropical Atlantic. The global ocean acts as an atmospheric CO_2 sink, taking up 23% of total anthropogenic CO_2 emissions (Friedlingstein et al., 2020) and causing ocean acidification (IPCC, 2019; 2021). The equatorial Atlantic Ocean is the second-largest source of CO_2 to the atmosphere after the equatorial Pacific (Landschützer et al., 2014; Takahashi et al., 2009). The concentration of atmospheric CO_2 is continuously increasing due to

55   human activities (IPCC, 2019; 2021), and characterizing the role of the ocean in mitigating climate change through CO_2 uptake is thus a key investigation. Previous works in this region examined the influence of the equatorial upwelling and of the Amazon plume on the CO_2 flux. CO_2-rich equatorial waters, originating from the equatorial upwelling (Andrié et al., 1986) strongly contrast with the CO_2 undersaturated Amazon River plume waters. The magnitude of the Amazon River discharge is unique in the global ocean. It represents as much freshwater as the next 7 largest rivers in the world combined and contributes to

60   almost 20% of global river freshwater input to the ocean (Dai & Trenberth, 2002). It therefore strongly impacts the physical, biogeochemical and biological properties of the coastal and the open ocean. Often overlooked, the Amazon River plume is an atmospheric CO_2 sink of global importance (Ibánhez et al., 2016). The plume carries water rich in silicate, nitrogen and phosphate into the tropical oceanic waters that are strongly depleted in nutrients. As water mixes and turbidity decreases, the primary producer's growth and associated biological drawdown are stimulated (Chen et al., 2012). Nitrogen is rapidly

65   consumed, and nitrogen fixation by diazotrophs becomes the main pathway of carbon sequestration in the plume

2

(Subramaniam et al., 2008). This strong carbon drawdown leads to a significant sink of atmospheric CO_2 (Körtzinger, 2003; Lefèvre et al., 2010). Not taking into account the Amazon plume would result in overestimating the tropical Atlantic air-sea CO_2 flux by 10% (Ibánhez et al., 2016).

70 The Amazon River's discharge reaches a minimum in December and progressively increases from January onwards. The plume extension is minimum in that season (Fournier et al., 2015) and as a result, it is the season of maximum salinity in the northwestern tropical Atlantic. The difference between the fugacity of CO_2 (fCO_2) in the surface ocean and in the atmosphere (ΔfCO_2) climatology over 1998-2015 divides the north-western tropical Atlantic into two regions (Figure 1a). The Amazon outflow region is particularly hard to reconstruct due to its strong variability and a severe lack of data. Waters located in the

75 southeasternmost part of the domain act as a strong source of CO_2 to the atmosphere. The source progressively transitions into a sink north of 10°N as waters get colder linked to the seasonal winter cooling. This situation is typical of a transition zone between equatorial and subtropical waters in winter (Landschützer et al., 2020, Figure 1a). The freshwater of the Amazon remains mainly confined to the continental shelf due to winds perpendicular to the coast as they travel northwestward into the Caribbean Sea (Coles et al., 2013). However, it has recently been documented that off-shore freshwater transport is often

80 present in February and significantly alters the physical properties of the region (Reverdin et al., 2021). This is partly due to the interaction of the NBC rings with the Amazon plume (Figure 1c). The ocean color signature of the Amazon (Muller-Karger et al., 1988) has been used as a tracer to delineate the rings, and better understand their generation, evolution and characteristics (Johns et al., 1990; Fratantoni & Glickson, 2002). For example, Figure 1b shows two filaments stirred by two large rings. The Amazon River also influences the surface temperature and salinity of the rings. They are considered warm-core rings but have

85 a warm SST anomaly in the first half of the year, and a cold one in the second half, because the anomaly is relative to the regional SST, with an extensive warm pool in late summer and autumn (Ffield, 2005). Their signature in salinity is therefore plume-dependent as well. Ffield (2005) reported that 3 out of 4 rings were surrounded by lower salinity water. This is also highlighted in February 2020 where an NBC ring stirs a plume of fresher water rich in chlorophyll-a toward the open ocean (Figure 1b,c). Salinity and chlorophyll-a are therefore critical to understand the surface physical and biogeochemical properties

90 of the region, as well as the air-sea fluxes of CO_2 (Figure 1).

The northwestern tropical Atlantic is a dynamically active region, containing eddies several hundred kilometers in diameter and connected to the world's largest river. There are surprisingly few biogeochemical observations available for winter months during low outflow from the Amazon River. Few tropical Atlantic measurements of biogeochemical tracers are available with

95 one transect in winter in the Surface Ocean CO2 Atlas (SOCAT, Bakker et al., 2016) database south of 10°N crossing the region. This scarcity is a major impediment in understanding the biological and physical processes underlying the oceanic carbon and nutrient cycles in the region. Satellite surface chlorophyll-a and salinity show a strong spatial structure, with eddies, filaments, and a fresh water plume (Figure 1 b,c). In this study, we take advantage of the physical and biogeochemical data

collected during the EUREC⁴A-OA/ATOMIC experiment in January-February 2020, combined with satellite data, to
100 understand how the NBC rings and their related structures impact the air-sea fluxes of CO_2 in winter.
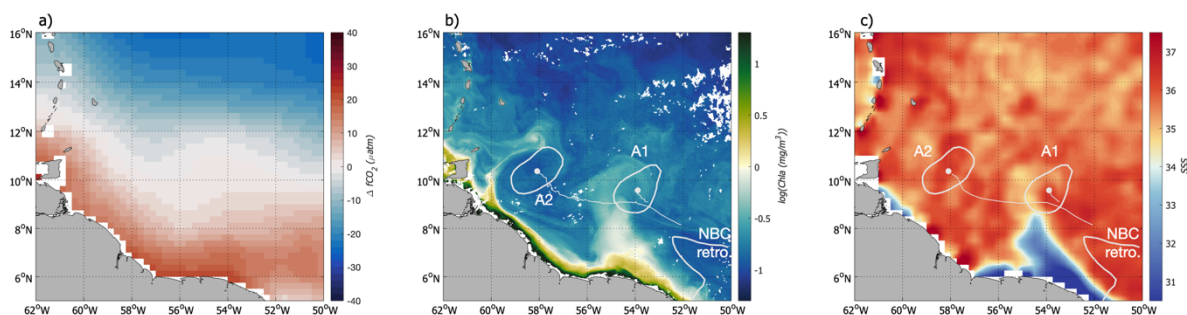

**Figure 1: ΔfCO2 February 1998-2015 climatology (Landschützer et al., 2020). b) Chlorophyll-a and c) SSS on Feb. 6th with the
contours of NBC rings A1 and A2 defined by the TOEddies algorithm (Laxenaire et al. 2018) from concurrent satellite Absolute
105 Dynamic Topography (ADT) field, their center and trajectory. The 0.51 m contour of satellite derived ADT represents the NBC
retroflection.**

The paper is organized as follows. We present the in-situ observational data from the EUREC⁴A-OA/ATOMIC experiment as
110 well as the satellite data in section 2. We identify the water masses observed in the region, their physical and biogeochemical
properties and estimate the CO_2 fluxes at regional scale using empirical relationships in section 3. We compare the results with
climatologies of CO_2 fluxes to evaluate the added knowledge brought by the intensive surveys of February 2020 and discuss
the interannual variability in section 4 followed by the conclusion.

2 Data and Methods

115 **2.1 In-situ data**

The EUREC⁴A-OA (Elucidating the Role of Clouds-Circulation Coupling in Climate Ocean-Atmosphere) / ATOMIC
(Atlantic Tradewind Ocean Mesoscale Interaction Campaign, Stevens et al., 2021) campaign took place in January and
February 2020 and involved research vessels (RV) from France (RV Atalante, Speich & The Embarked Science Team, 2021),
Germany (RV Maria S. Merian, hereby designated as Merian, Karstensen et al., 2020 and RV Meteor, not considered in this
120 study since no CO_2 measurements were taken onboard), and the United States (RV Ronald H. Brown, hereby designated as
Ron Brown, Quinn et al. 2021). These cruises provided numerous in-situ measurements and, in this study, we will focus on
the continuous near surface measurement of temperature, salinity, fCO_2 and winds.

Temperature, salinity from thermosalinographs (TSG), as well as fCO$_2$, were measured from water pumped ~5 m below the
surface (Figure 2 a,b,c, ΔfCO$_2$ from measured fCO$_2$). For each ship, the resulting CO$_2$ data is corrected (Lefèvre et al., 2010;
Pierrot et al., 2009) from the temperature difference between the water at the ship's water intake and the one analyzed by the
instrument. On RV Atalante, underway oceanic and atmospheric fCO$_2$ were detected by infrared detection using a Licor 7000
(Olivier et al., 2020). The fCO$_2$ system was the same as in Lefèvre et al. (2010). It uses an air–sea equilibrator described by
Poisson et al. (1993). Seawater from the TSG pumping circuit circulates in the equilibrator at a rate of 2 L.min^{-1}. A closed-
loop of about 100 ml of air flows through the equilibrator designed to avoid bubbles at the air–sea interface. To minimize
temperature corrections, the equilibrator is thermostated with the same seawater as the one used for CO$_2$ measurements. The
temperature difference between the equilibrator and the sea was on the order of 0.5 °C.

Furthermore, 138 samples for dissolved inorganic carbon (DIC) and total alkalinity (TA) analysis were collected onboard RV
Atalante as well as inorganic nutrients (silicate, phosphate, nitrate and nitrite).

An OceanPackCUBE ferrybox system from SubCtech was installed on the RV Merian measuring continuously the oceanic
fCO$_2$. Water is pumped at a rate of ~7 l/min through a debubbler unit subsequently followed by a SeaBird SBE 45
thermosalinograph before it circulates along a membrane through which CO$_2$ diffuses. On the other side of the membrane, the
air-loop is circulated at a rate of 0.5 l/min through a Li-COR LI840 non-dispersive infrared gas analyzer (e.g., Arruda et al.,
2020). On RV Ron Brown the General Oceanic Inc. 8500 pCO$_2$ instrument follows a similar methodology to the underway
fCO$_2$ system deployed on the Atalante and is detailed in Pierrot et al. (2009).

Wind measured by the weather stations of each research vessel is adjusted using a logarithmic wind velocity profile to represent
the wind at 10 m height above sea level which is used to compute the air-sea CO$_2$ fluxes.

An intercomparison of the fCO$_2$ measured by the RVs Atalante and Merian is attempted when the ships were located at a
distance inferior to 5 km (Figure 2d). On average, the fCO$_2$ measured by the RV Merian is 6.4 µatm higher than the one
measured on the RV Atalante, with a standard deviation of 4.8 µatm. The RVs Merian and Ron Brown crossed the same water
mass at 13-14°N/57°W on February 12th. On average, the RV Merian fCO$_2$ is 6 µatm higher than the RV Ron Brown fCO$_2$. In
part we link these differences to the slower response time of the membrane system, however differences also lie within the
uncertainties of the fCO$_2$ observing systems (~5µatm for the membrane system installed on the RV Merian (see Arruda et al.,
2020) and ~2 µatm for the equilibrator systems installed on the RVs Atalante and Ron Brown). The region where RV Merian
and RV Atalante were very close is very variable (standard deviation of 20 µatm), and the RV Merian and RV Ron Brown
were never in the same place at the same time, so that the observed differences could also be due to the natural variability of
fCO$_2$ sampled differently by the various ships. Hence, we did not apply any correction and we checked that the effect of a 6
µatm systematic bias on the RV Merian fCO$_2$ has a minor effect on our resulting interpolations. It would lead to less than 2
µatm difference on our mean interpolated fCO$_2$ and less than 0.1 mmol.m^{-2}.day^{-1} on the mean derived air-sea CO$_2$ flux.

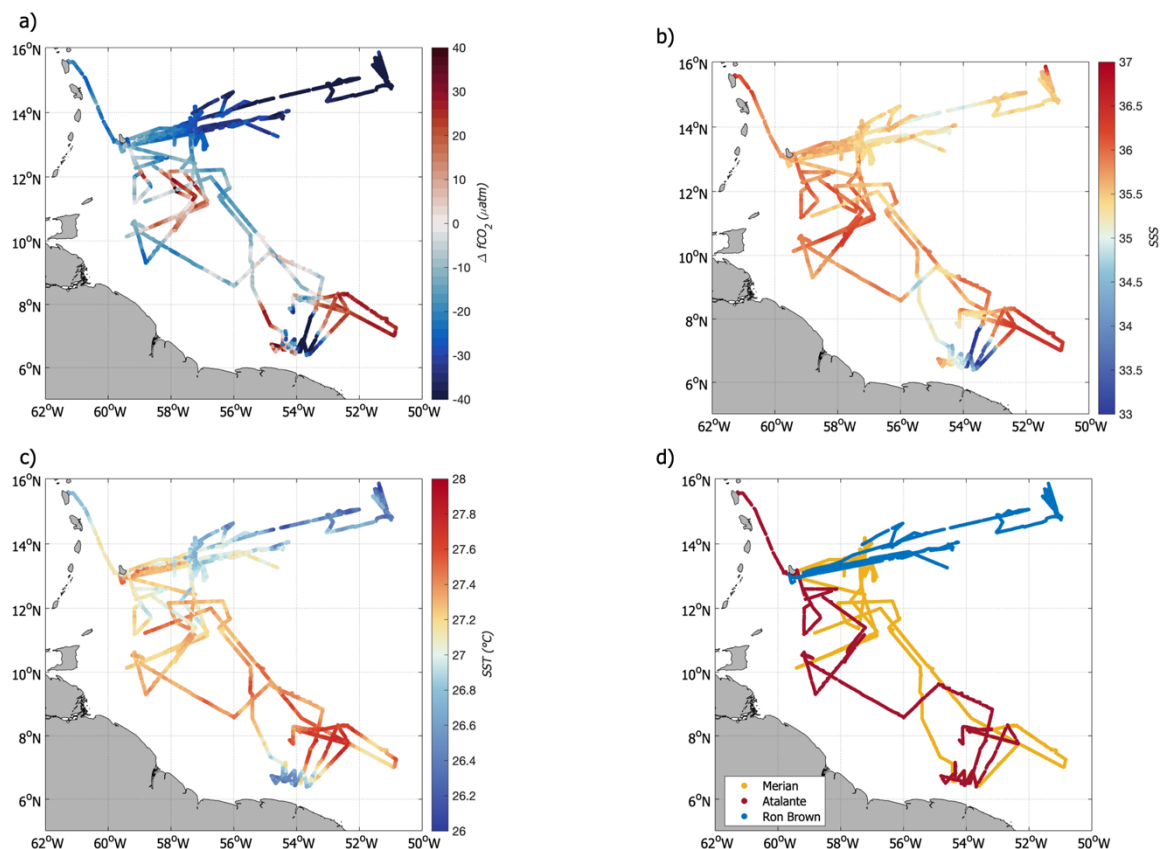**Figure 2: In-situ measurements of surface (a) ΔfCO2, (b) salinity and (c) temperature. The Merian, Atalante and Ron Brown ship tracks are presented in (d).**

2.2 Satellite and atmospheric reanalyzes data

160   Daily satellite maps of chlorophyll-a (Chl*a*), sea surface temperature (SST), as well as absolute dynamic topography (ADT) and sea surface salinity (SSS) are used in this study.

The salinity maps are a blend of the Soil Moisture Ocean Salinity (SMOS, Jan. 2010-present), and Soil Moisture Active Passive (SMAP, Apr. 2015-present) measurements developed by Reverdin et al. (2021) and optimized for the northwestern tropical

165   Atlantic in February 2020 (Figure 1c). The European SMOS and US SMAP missions observe the sea surface by L-band radiometry from sun-synchronous polar-orbiting satellites (Entekhabi et al., 2010; Font et al., 2009; Kerr et al., 2010; Piepmeier et al., 2017). Combining 6 a.m. and 6 p.m. measurements of both missions provides an almost complete coverage each day.

6

When the coverage was not complete over our region, the 6 a.m. track of the following day was also included. This daily field is available for the first 20 days of February, and leaves out only 2 days without sufficient coverage to retrieve salinity data. It

170   has a spatial resolution close to 70 km, and an uncertainty on the order of 0.5 pss. The product, its uncertainties and the comparison between the TSG salinity and the SSS product are detailed in Reverdin et al. (2021).

Daily Chl*a* concentration maps and SST maps are produced by CLS (Stum et al., 2016) on a spatial grid of 0.02°. The Chl*a* concentration maps are composites built from VIIRS (on Suomi-NPP and NOAA-20 US platforms) and OLCI (on Sentinel

175   3A and 3B Copernicus European platforms) satellite sensors. The SST product is a 1-day average of 4 infrared radiometer satellite data. Both datasets are sensitive to the cloud cover, but during our period of interest, they are usually without many gaps except at the end of February. Comparison between the TSG SST and the satellite SST product are detailed in the RV Atalante cruise report (Speich & The Embarked Science Team, 2021).

180   Daily ADT maps at a ¼° resolution combine data from all satellites available for the period 1993 to present. From these ADT maps, the TOEddies algorithm, developed by Laxenaire et al. (2018), identifies eddies and their trajectories (Figure 1). The eddy detection is based on the closed contours of ADT, as well as the maximum geostrophic velocity associated to the eddy.

In order to compute the air-sea CO_2 fluxes, the European Centre for Medium-Range Weather Forecasts (ECMWF) Reanalysis

185   v5 (ERA5) hourly wind speed and mean sea level pressure, P_{atm}, is used. ERA5 covers the period from January 1950 to present, and provides hourly data on a 30 km grid. In addition, the monthly wind speed and SST fields over the period 1998-2015 are used, and a climatology over this period is computed. The wind speed in the region in winter is on average between 6 and 8 m/s and its variability is low.

190   We compare the EUREC[4]A-OA/ATOMIC observations with the observation-based CO_2 partial pressure (pCO2) climatology developed by Landschützer et al., (2020), created using a 2-step neural network method (Landschützer et al., 2016) and combining open and coastal ocean datasets. The associated ΔpCO_2 and air-sea CO_2 flux monthly field climatologies over the 1998-2015 period are computed using the ERA5 climatological wind, SST and P_{atm} fields as well as the atmospheric CO_2 from the Ragged Point, Barbados station.

195   **2.3 Methods**

2.3.1 Air-sea CO2 flux

We compute the air-sea flux (F; mmol.m^{-2}.day^{-1}) as:

$$F = k \cdot K_0 \cdot (fCO_2 - fCO_{2atm}) \tag{2}$$

7

Where K_0 is the solubility of CO_2 is seawater, expressed as a function of SSS and SST by Weiss (1974); fCO_{2atm} is the

200   atmospheric CO_2 fugacity; and k is the gas transfer velocity. k is calculated following the relation from Wanninkhof (2014):

$$k = 0.251 \cdot < U^2 > \cdot (Sc/660)^{-0.5} \tag{3}$$

where Sc is the Schmidt number and U is the wind speed at 10 m above sea level measured by each ships weather station or

derived from ERA5 wind speed. The measured winds from the ships are used to compute the along-track flux, while the ERA5

wind speed is used for the satellite-based analysis and the air-sea CO_2 flux climatology.

205   In order to compute fCO_{2atm} over that period, we first derived the saturation vapor pressure (P_{H2O}) then the atmospheric pCO_2

using the monthly averaged CO_2 mole fraction (xCO_{2atm}) measured at the NOAA/Earth System Research Laboratory (ESRL)

station in Ragged Point, Barbados (13.17°N, 59.43°W):

$$fCO_{2atm} = xCO_{2atm} \cdot (P_{atm} - P_{H20}) \cdot C_f \tag{1}$$

Where P_{H2O} is the saturation vapor pressure computed from SSS and SST, and C_f is the fugacity coefficient, function of the

210   atmospheric pressure and SST (Weiss, 1974).

2.3.2 Reconstruction of fCO₂ from satellite maps

We observed that in the northwestern tropical Atlantic in winter the in situ fCO_2 strongly depends on SST, SSS and surface

Chl*a* (Figure 3). There is a strong positive dependence of fCO_2 on SSS, with low fCO_2 for low SSS (Figure 3a). Across the

215   whole EUREC⁴A-OA/ATOMIC region, SST did not vary much (mean SST of 27°C, and standard deviation of 0.5°C), but

warmer waters present higher fCO_2. The dependence on Chl*a* allows for the discrimination of water masses with the same

surface TS properties but not the same fCO_2. fCO_2 is not only influenced by ocean dynamics and chemistry, but also by marine

biology. The biological carbon pump is one of the major components of the oceanic and global carbon cycles, as the

photosynthetic production of organic carbon by marine phytoplankton accounts for about half of the carbon fixation associated

220   with global primary production (Arrigo, 2007; Behrenfeld et al., 2006; Field et al., 1998). Satellite-based Chl*a* is hard to

discriminate from detrital material in areas were both are present and have the same wavelength. Figure 3 shows that waters

with a SST of 26.5°C and SSS between 35-36 can either be rich in Chl*a* and have a high fCO_2 or low in Chl*a* and have a low

fCO_2. Waters rich in detrital material tends to limit the phytoplankton growth and microbial respiration of riverine material on

the continental shelf likely dominates (Aller & Blair, 2006; Medeiros et al., 2015; Mu et al., 2021). This relationship is analyzed

225   in more detail for the different water masses identified in the region in parts 3.2. and 3.3. Chl*a* was not measured onboard,

thus, we use satellite surface Chl*a* co-located along the ship track.

Our approach is to derive from this large dataset a relationship linking fCO_2 to SST, SSS and Chl*a* in order to provide maps

of fCO_2 based on the satellite maps of SST, SSS and Chl*a*. Even considering the extend of the EUREC⁴A-OA atomic cruise,

230   the dataset is still sparse, and cannot fully represent the small-scale variability it highlights. In order to understand the fluxes

at regional scale the need for a good spatial resolution arises. For that, the surface T-S-Chl*a* diagram computed from the ship

measurement (and collocated satellite Chl*a*) is interpolated using a linear 3D interpolation on a grid of SST, SSS and Chl*a*.
The grid has a resolution of 0.01°C in SST, 0.1 in SSS, and 0.01 in log(Chl*a* (mg/m^3)). Using a 3D linear interpolation to
mapping the fCO$_2$ data over a grid is a simple yet effective solution for a dataset that is still relatively sparse. The method is

235   presented in more details in the supplementary materials (Text S1). Using a linear fit prevents from oscillations between two
data points, and yields good results. Along the ship track, the standard deviation between the measured and reconstructed fCO$_2$
is of 4 µatm. To each triplet of surface T, S, and log(Chl*a*) in the range of the values measured by the ship is therefore associated
a value of fCO$_2$ based on the 3D linear interpolation of the in-situ values. In order to cover the whole range of T-S-log(Chl*a*)
present in the region, we extrapolate to lower temperatures and lower salinities than the ones measured by the ship. In order to

240   do so, we add 4 points to the T-S-Chl*a* diagram at lower salinities and lower temperatures based on previous knowledge of the
region. For the low salinity domain (SSS < 30), fCO$_2$ is strongly dominated by salinity and the influence of temperature is
weak (Lefèvre et al., 2010). The SSS-fCO$_2$ relation developed by Lefèvre (2010) is in good agreement with the SSS-fCO$_2$
relationship computed from this study data (supplementary Figure S1) in the common range, we therefore use it to compute
fCO$_2$ at a salinity of 26 (fCO$_2$(S = 26) = 251.4 µatm). The lower temperature is mostly located in the northern part of the

245   domain, that is the least variable and where the variations of fCO$_2$ are dominated by the ones in temperature. From this dataset
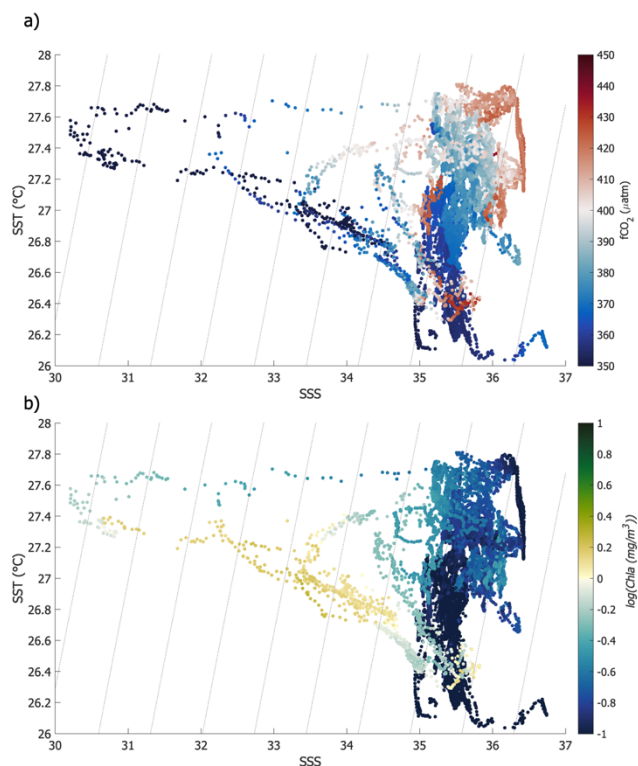

Figure 3: Surface TS diagram, color-coded with fCO$_2$ (a) and Chl*a* (b).

Biogeosciences
Discussions

we compute a variation of 15 µatm/°C, which is consistent with the 4.23% °C^{-1} expected variation of fCO_2 with temperature due to the temperature sensitivity of the carbonate dissociation constants and CO_2 solubility (Takahashi et al., 2002; Wanninkhof et al., 1999). We use this dependency to compute the fCO_2 at a temperature of 24°C to extend cover the whole range of temperature in the region.

250

We combine the interpolated fCO_2 with satellite maps of SST, SSS and Chl*a* to obtain daily high-resolution maps of fCO_2. Some days, either the presence of clouds altering the Chl*a* and SST or the lack of salinity coverage prevent the retrieval of fCO_2. In order to limit the error on fCO_2, we only keep 9 days out of the 20 first days of February (2, 4, 6, 7, 9, 11, 12, 17 and

255 19 of February) where the coverage is sufficient. Then, daily mean sea level pressure maps and wind fields are used to compute the air-sea CO_2 flux over the region in a similar way as described in 2.3.1. The salinity maps present major errors near islands, because no correction of the island effect on the SMAP maps (Grodsky et al., 2018) was applied. Therefore, the reconstructed flux will be studied over a region excluding the close vicinity of the islands [59°W-50°W, 5°N-16°N].

260 **3 Results**

3.1 A transition region presenting a strong mesoscale activity

Figure 2a presents the ΔfCO_2 measured during the EUREC[4]A/ATOMIC campaign in January-February 2020. It shows a complex environment that presents similar large-scale features as the climatology, but it reveals numerous smaller scale structures (Figure 1a). Among the latter, two stand out. These are the very low fCO_2 in the south-eastern part of the domain,

265 and the high fCO_2 around 11°N. Winter is often considered as a period of low variability in the western tropical Atlantic, however, it is still a highly dynamic region. The northwestern tropical Atlantic is commonly divided into two parts, the northern much less variable part (also called "Trade wind region"), and the southern part, also referred as Eddy Boulevard (Stevens et al., 2021). In early 2020, the NBC retroflection was very variable and shed two large anticyclonic rings (Figure 1b,c). They are long-lived 250-km large eddies traveling north-westward toward the Caribbean in the Eddy Boulevard region. The ring

270 detection algorithm TOEddies based on ADT indicates that NBC ring A2 separated from the retroflection in late December, was fairly stationary during the cruise period (February 2020) and located around 58°W-11°N. NBC ring A1 separated from the retroflection in early February 2020 and then stayed around 54°W-10°N for 10 days before translating northwestward toward the Caribbean after the 20th of February. These eddies contribute to the variability of the region in two ways. As they travel, they transport the water trapped in their core during their formation, but they also stir the surrounding waters.

Biogeosciences
Discussions
Open Access
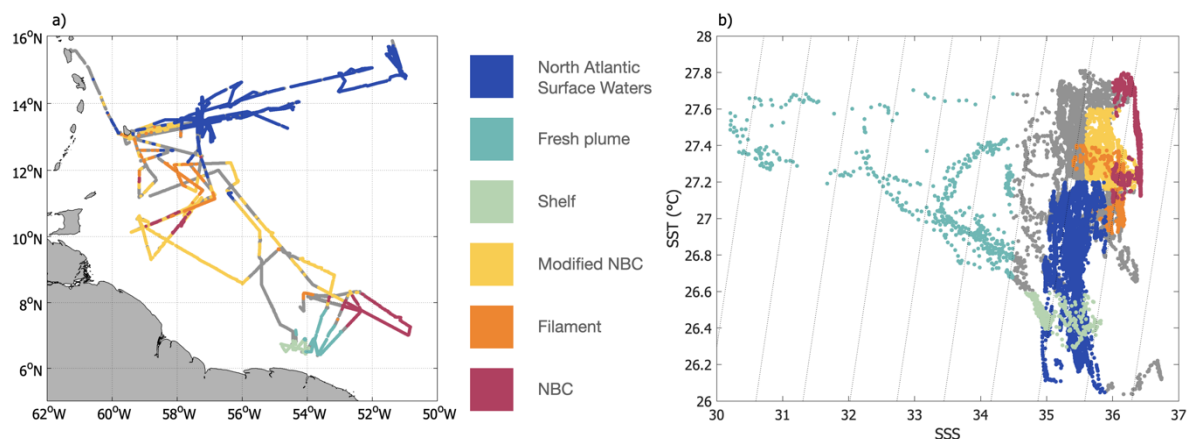
EGU

3.2 Surface water masses identification

Figure 4: a) Map representing the RVs Atalante, Merian and Ron Brown ship tracks color-coded with the identified water masses. b) T-S diagram color-coded with the water masses; the gray color corresponds to points that do not fit into the definition of the identified water masses.

In order to better understand the variability of the region, it is necessary to characterize the main water masses present in winter. From SST and SSS only, we are not able to define water masses with a unique fCO_2 signature (Figure 3). By combining SST and SSS with Chl$a$ and using information from the dynamical structures of the region, we identified six upper-ocean water masses (Figure 4). For example, the fresh plume water mass corresponds to low SSS, while the NBC water mass is associated to warm SST, high SSS and low Chl$a$ (Figures 3 and 4) in the region of the retroflection and eddy formation. The along track ΔfCO_2 for each ship is presented on Figure 5, color-coded with the identified water mass, highlighting the link between the surface T-S-Chl$a$ relation and ΔfCO_2. In this first part, we will present the two surface water masses that are usually identified in the region (e.g. Longhurst et al.,1995, 2010) and their physical properties. We will introduce four new ones in the following parts, as well as their associated dynamic structures.

North of Barbados, the domain is mostly dominated by North Atlantic Subtropical Waters. They have a SSS in the range of 35 to 36 and are relatively cold (SST < 27.2°C). Their SST diminishes over time towards the end of February. These waters are less influenced by coastal dynamics and therefore are not very productive at the surface (Chl$a$ levels inferior to 0.14 mg.m^{-3}) due to low nutrient levels. They are mainly located north of 13°N, and get progressively colder toward the north-east. The RV Ron Brown stayed in that Trade Wind region for almost a month (Figure 5). The observations collected from this ship show NASW lower fCO_2 with respect to the atmosphere ($\Delta fCO_2 = - 40\mu$atm). Similar results are found on one of the RV Merian's transect, with $\Delta fCO_2 < - 30\mu$atm.

The surface-intensified NBC is fed by the central branch of the South Equatorial Current (SEC, Schott et al., 1998). As the cold and saline water from the upwelling region is transported westward by the SEC, it warms up (SST > 27°C), but retains its saline characteristic (SSS > 36) as it reaches the NBC retroflection region (Figure 4). This NBC water mass is oligotrophic

11

300   (Figure 3b), and therefore in our area of interest distinguished itself by its low level of surface Chl*a* (Chl*a* < 0.14 mg.m^{-3}).
These waters are found in the retroflection area, and sampled by both RVs Merian and Atalante at the beginning of February
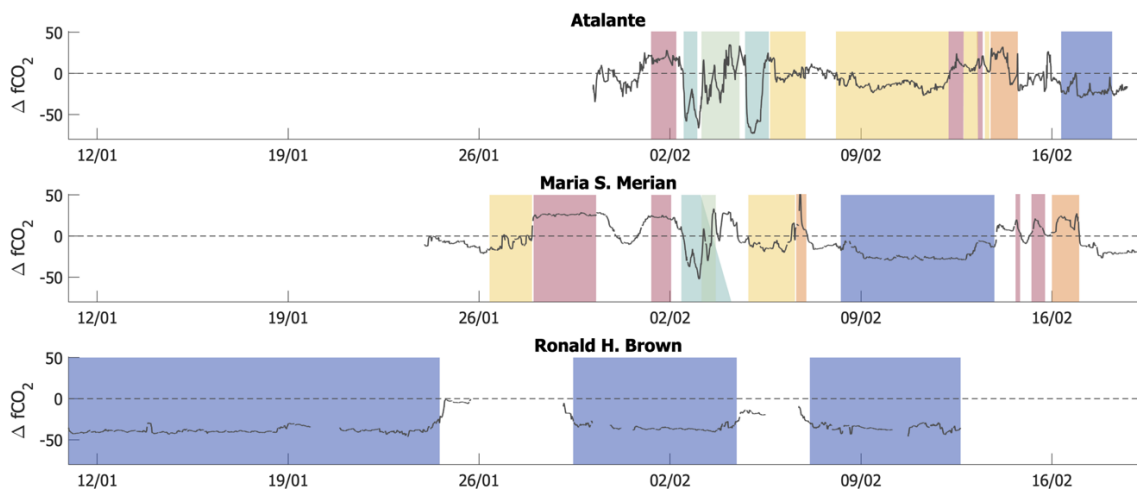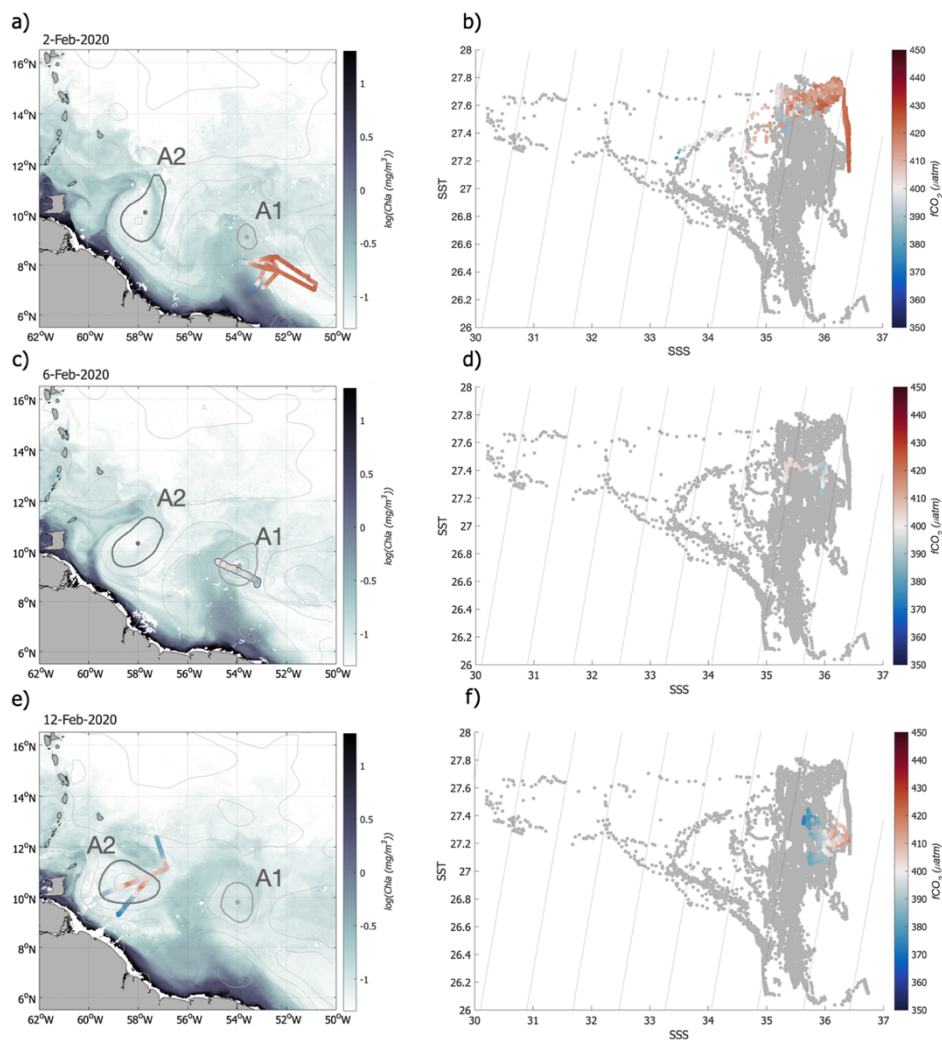(Figure 5).

**Figure 5: RVs Atalante (top), Merian (middle) and Ron Brown (bottom) ΔfCO$_2$ time-series. The background color
indicates the crossed water mass domains (see definition in legend of Fig 4).**

3.3 North Brazil Current rings

305   The extension of the NBC retroflection varies depending on the state of eddy formation. It moves northwestward up until 9°N
as an eddy is forming, and then retracts to the southeastern part of the region. During our period of interest, the retroflection
shed anticyclone A1 at the beginning of February. It is difficult to estimate the date of shedding as the area is highly dynamic
and detecting the first closed contour of ADT is complicated and may be inaccurate. It is however interesting that the two ships
sampled the retroflection when it was expanding to generate A1, and this northwestward expansion is well observed on several
310   physical and biogeochemical parameters (Figure 6a). RV Merian crossed the retroflection on January, 27th and stayed in the
area until February, 2nd (Figure 5). Chl*a* present on the shelf is advected by the strong currents on the periphery of the
retroflection and delineates well its south-western side (Figure 6a). The NBC waters stand out on the surface TS diagram, as
they are the most saline waters observed in the region (Figure 6b). They are also high in fCO$_2$ which reflects their equatorial
origin. Their SST is relatively warm, varying from 27.8 °C at the crossing of the first retroflection front, to 27.2 °C. The region
315   is rather homogeneous, with an almost constant SSS of 36.3 and ΔfCO$_2$ along the multiple crossings, as observed on the Merian
and Atalante transects (Figure 5). On average along those transects, the NBC fCO$_2$ is higher than fCO$_{2atm}$ by 20 μatm.

12

Anticyclone A1 is further crossed by the RV Atalante on February 6th, just a few days after its separation from the retroflection
(Figure 6c). The surface signal is almost lost, both in SST and in fCO2 (Figure 6cd). It is mainly composed of modified NBC
320 water, which properties are close to the NBC water (high SSS, high SST, low Chl*a*) but not as pronounced. This water mass
covers a larger area, which mainly encompasses the Eddy Boulevard region. It is defined here as SSS > 35.6, 27.16 °C < SST
< 27.6 °C and 0.11 mg m^{-3} < Chl*a* < 0.25 mg m^{-3}. While the high Chl*a* water delimits the retroflection area, it partly covers
the eddy A1.

325 **Figure 6: a) RVs Atalante and Merian ship track in the NBC retroflection (Merian: Jan. 27th to Feb. 2nd, Atalante: Feb 2nd), c) in
NBC ring A1 (Atalante: Feb 6th) and e) in NBC ring A2 (Atalante: Feb 12th-13th, Merian: Feb 13th-14th) color-coded with fCO2. The
background represents the Chl*a* on Feb 2nd (a), Feb 6th (c) and Feb 12th (e), and the contours of NBC rings A1 and A2 are indicated.
b),d),f) Corresponding T-S diagrams color-coded with fCO2.**

330

NBC ring A2 presents a different situation. Detached from the retroflection in early December 2019 (as defined from altimetry detection), it travelled north-westward while retaining an intense coherent core. Coastal waters identified by their high Chl*a* content were less present and mostly entrained at the north-westward edge of the eddy. After two months, A2 almost reached Trinidad and Tobago and was located around 11°N/58°W when it was sampled by the two ships (Figure 6e). The SST signal

335 is eroded, and most of the eddy is mostly made of modified NBC water with relatively low fCO_2. However high SSS (36.5) and fCO_2 (415 µatm) are still visible near the eddy center on the two crossings made by RV Atalante on the 12th and 13th of February. This is confirmed by the two sections of the Merian that crossed the altimetric eddy center and measured SSS 0.5 higher in the 50 km radius around the center and above 36. The NBC water mass is therefore found close to the center of eddy A2, as well as its associated high fCO_2.

340

From the collected observations, it appears that the surface signature of NBC rings is relatively variable and complex. It is well marked in their formation area in the NBC retroflection, where waters brought north by the NBC are warmer, saltier, and higher in fCO_2 than the water of the northwestern tropical Atlantic. As the eddies travel northwestward, further away from the retroflection, they may be subject to various processes that modify the surface signal. Unfortunately, the data collected is not

345 sufficient to shed light on which processes involved in this situation. South of Barbados, away from the retroflection, the modified NBC is therefore the most common water mass. Nevertheless, the NBC water is still sometimes observed months after the separation from the retroflection, in the eddy center.

3.4 Freshwater plume

350 The NBC rings form and evolve in an area highly influenced by the Amazon River plume. Even if February is a period of low Amazon River outflow (Dai & Trenberth, 2002), freshwater events are relatively common. In February 2020, a freshwater plume detached from the Guiana plateau and spread out into the northwestern tropical Atlantic. The off-shelf plume was steered northward by the retroflection and NBC ring A1 up to 12°N and then extended westward toward the Caribbean Sea. Waters carried by the plume strongly contrast with the saline waters of the retroflection. They include water from the Amazon and

355 present low SSS (SSS < 34.5), low fCO_2 (fCO_2 < 380 µatm) and high Chl*a* (Chl*a* > 0.25 mg m^{-3}). The plume was crossed three times, twice on February 2nd and once on February 5th (Figure 5). Freshwater from the Amazon arrived on the plateau on the 1-2nd of February and was then entrained northwestward by Ekman transport and geostrophic currents (Reverdin et al., 2021). On the 2nd of February RVs Atalante and Merian left the retroflection area to cross the adjacent nascent plume. SSS rapidly decreased, reaching 33 which is associated to a strong decrease of fCO_2 (Figure 7). From the 2nd to the 5th of February, the

360 plume formed and on February 5th the plume is approximately 100 km wide, with lowest salinities around 30. Based on satellite SSS data of the following days, the plume appears to have reached even lower salinities and then spread out over the north-western tropical Atlantic. It first spread northward, steered by A1 and then northwestward, channeled between A1 and A2

reaching all the way up to 12°N and extending over more than 100 000 km² (Reverdin et al., 2021). The plume can be followed by satellite SSS and Chl*a* maps (Figures 6a, c, e). Indeed, the low SSS is also accompanied by Chl*a* as water from the Amazon

365 are considered highly productive. The north-western tropical Atlantic is in general nutrient-limited but the nutrients brought by the Amazon can support the occurrence of a bloom. The plume is also characterized by high silicate (between 4 and 10 μmol kg⁻¹ in the plume), while nitrate and phosphate are rapidly consumed. Traces of inorganic phosphorus were observed in the plume, while nitrates were absent from surface waters (Supplementary Figure S2). Low salinity combined with high biological productivity led to low fCO$_2$ and a strong carbon drawdown in the plume, as the ΔfCO$_2$ reached -73 μatm on

370 February 5th (Figure 5).

In an area highly influenced by the NBC waters, through rings or the retroflection, the plume stands out and modify the biogeochemical dynamics of the region.
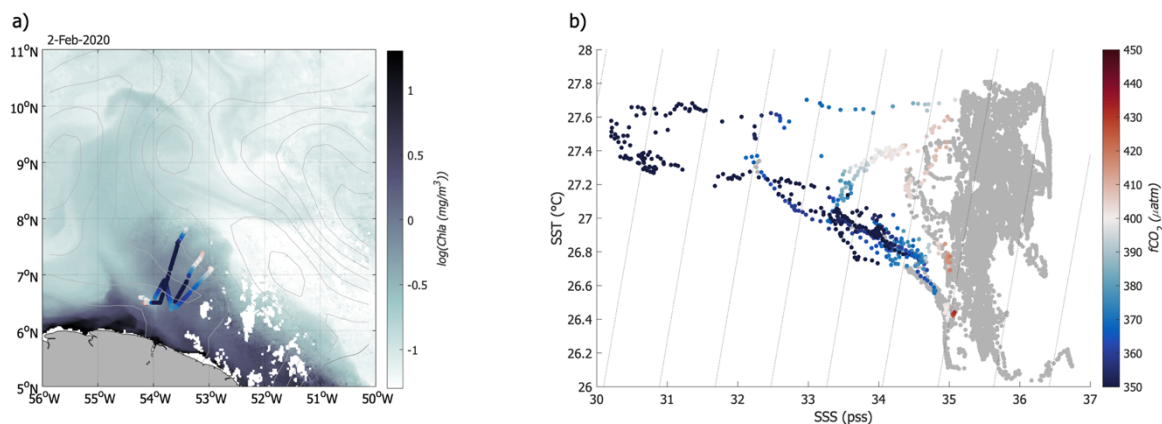
Figure 7: a) RVs Atalante and Merian ship track in the freshwater plume (Atalante: Feb 2nd, Feb 5th, Merian: Feb 2nd) color-coded
375 **with fCO$_2$. The background represents the Chl*a* on Feb 2nd. b) Corresponding T-S diagram color-coded with fCO$_2$.**

3.5 Coastal water and filaments

The freshwater plume is not the only water stirred by the NBC rings travelling from the NBC retroflection towards the Caribbean. The shelf water is very different from the plume water, and was only sampled sparsely on the way in and out of the

380 plume (Figures 4,5). On the Guiana plateau water is very rich in Chl*a* and detrital material, rather saline (SSS ~ 35.5) and relatively cold (SST ~ 26.5°C) (Figure 4). Since the water sampled on the edge of the plume was cold due to a local upwelling event (or vertical mixing event) detailed in the supplementary materials (Figure S3), temperature is not homogenous on the shelf.

Further north, a filament is stirred on the western side of NBC ring A2 (Figure 8a). It is a small-scale structure, approximately

385 10 km wide, easily identifiable due to its high Chl*a*. The filament is continuously stirred by A2, and so is already visible on

Chl$a$ maps of February 2nd (Figure 6). It followed A2 westward's translation and was crossed on February 6th and 17th by RV Merian, and on February 14th by RV Atalante (Figure 5). It has a SSS close to 36, and an SST between 27°C and 27.5°C, thus it is slightly colder and more saline than its surrounding waters (Figure 7b). It stands out by its high Chl$a$ content (Chl$a > 0.25$ mg m^{-3}), even if this is lower than close to the coast or in the freshwater plume. The strongest signal is observed on the ocean

390 carbon parameters. In contrast to the freshwater plume, this filament presents very high fCO$_2$ (> 430 µatm), highlighting different origins. It stands out from the ship track time series by also having a larger positive ΔfCO$_2$ (50 µatm). Whereas the freshwater plume observed more southeastward carries water recently arrived on the plateau from the Amazon, the northwestward filament contains shelf waters.
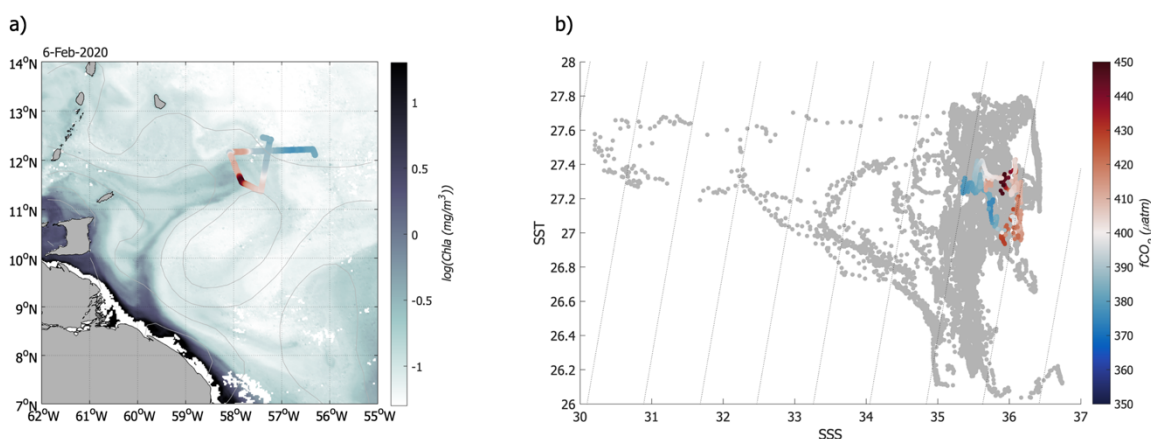
395 **Figure 8: a) RV Merian ship track in the shelf water filament (Feb 6th) color-coded with fCO$_2$. The background represents the Chl$a$ on Feb 6th. b) Corresponding T-S diagram color-coded with fCO$_2$.**

3.6 CO$_2$ air-sea flux

In order to better characterize the impact of each structure on the regional flux, we computed air-sea CO$_2$ maps from satellite
400 data, at a resolution higher than 60 km (Figure 9), averaged over the period of the cruise (February 2nd to February 19th). The along-track flux represented on Figure 9a and the reconstructed regional field (Figure 9b) show the importance of the small-scale dynamical structures, and highlights two strong regimes that are found on the reconstructed map. The air-sea CO$_2$ flux in the northeastern part of the domain, characterized by the NASW, is mainly dominated by temperature effects while further south the presence of NBC rings, and their interactions with shelf waters, create a strong dependence of the CO$_2$ flux on SSS
405 and on the biological and biogeochemical processes highlighted by Chl$a$.

We evaluate the integrated air-sea CO$_2$ flux over the region. In February, waters are the coldest, and the region is a strong CO$_2$ sink of -1.7 TgC month^{-1} (Figure 10). Three biogeochemical domains mainly contribute to the air-sea CO$_2$ flux, the NASW,

the freshwater plume and the NBC retroflection. The impact on the flux of the small-scale coastal filament is evident along the
410   ship tracks (Figure 9b). However, its contribution to the total flux is weak as the signal is smoothed when averaging over
February, as the filament moves following the A2 ring northwestward translation. Each of the main three regions is defined
based on its averaged SST, SSS and Chl*a* properties in February and the region-specific flux is determined (Figure 10).
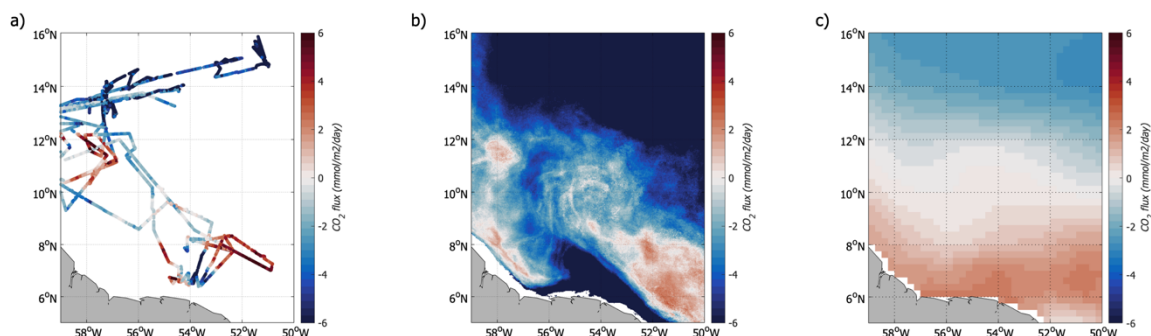
Figure 9: a) Air-sea CO$_2$ flux measured in Jan-Feb 2020 during the EUREC^{4}A-OA/ATOMIC cruise. b) Air-sea CO$_2$ flux
415   **reconstructed over February 2020. c) February climatology of the air-sea CO$_2$ flux over 1998-2015 (Landschützer et al., 2020).**

NASW contributes to about 60% of the total sink due to their relatively cold temperature and to strong winds that enhances
the air-sea exchanges. These waters extend from Barbados northward and eastward, cover more than 1/3 of the domain and
420   show a weak variability over the month of February.

The NBC retroflection is a source of CO$_2$ to the atmosphere. In February, the strongest signal is observed in the southeastern
part of the domain up to 8°N/53°W. The retroflection nevertheless impacts the region as far as 10°N/54°W as it is spatially
variable, reaching up to 10°N when shedding an eddy. NBC rings present a small positive February air-sea CO$_2$ flux average.
425   Eddy A1 is almost stationary from its formation date (around February 6th) until February 20th and its neutral to slightly positive
CO$_2$ flux is centered around 10°N/54.5°W (Figure 9). Eddy A2 translates rapidly westward at the beginning of February, and
then northward from the 15th of February. Its signal is therefore not as visible as on the ship tracks as it is averaged over one
month. The retroflection is the main region with a positive air-sea CO$_2$ flux, even if the region is too small to have a big global
impact, understanding small-scale features may be significant for the total flux. The NBC rings carry part of the signal, which
430   is heavily modified as they travel northwestward. As a result, on average for the month of February only the retroflection
maintains a positive flux, while a large part of the domain dominated by modified NBC waters (non-influenced by the plume)
behaves as a small sink.

The freshwater plume with Amazon water is nascent when crossed by the ships (Figure 9b), but is already the strongest signal
435   of the time-series. As the plume develops, it is entrained by NBC ring A1, then A2 and spreads out into the open ocean, as
observed on SSS and Chl*a* maps. The plume generates a strong CO_2 sink that is amplified by strong winds, and reaches up to
12°N (Figure 9). The freshwater plume covers only 10% of the total area, but contributes to almost 20 % of the sink. In winter,
this region is either not characterized in previous studies, or considered as dominated by high fCO_2 waters brought by the NBC
on the climatology. We observe here that the direct effect of NBC rings in transporting CO_2-rich waters is relatively weak in
440   winter, and the main signal is associated to the filaments they stir.

The north-western tropical Atlantic therefore behaves as a sink of CO_2 in February, driven by the cold north Atlantic
subtropical waters and the Amazon freshwater plume stirred by NBC rings.
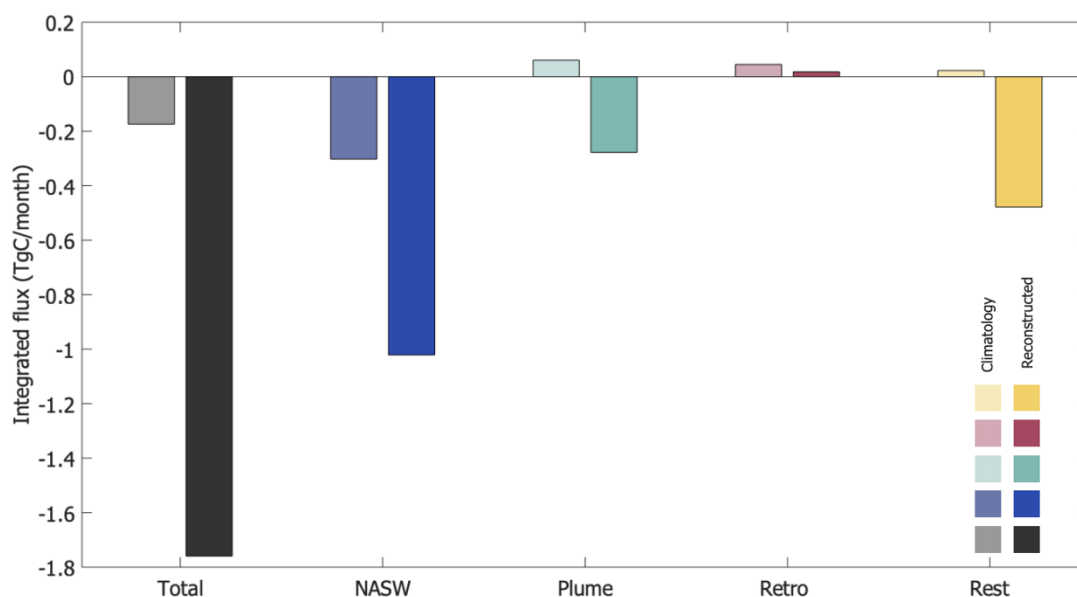
445   **Figure 10: Integrated flux for the [5°-16°N, 59-50°W] domain, and for 3 water masses. For each bar duet, the one on the left in faded
colors represents the integrated flux from Landschützer et al., (2020) February climatology, while the one on the right is computed
from the reconstructed flux. Same color code as in Figure 4.**

4 Discussion

4.1 Biogeochemical provinces

In an effort to understand how biogeochemistry is forced by physical processes in the ocean and atmosphere, we used surface Chl*a* to complement SST and SSS data in defining surface water masses. Partitioning the world ocean into biogeochemical provinces based on physical, geographical and biological criteria has long been proposed to study and better understand biological processes (Fay & McKinley, 2014; Longhurst et al., 1995; Longhurst, 2010). As reviewed by IOCCG (2009), satellite Chl*a* has been widely used to determine biogeochemical provinces, a term coined by Platt et al. (1991) and associated biological primary production but relatively few studies have used such methodologies for mapping air-sea CO_2 fluxes. Recently, Landschützer et al. (2013, 2016) have divided the world ocean into biogeochemical provinces for deriving fCO₂ and air-sea CO_2 fluxes. The way we defined water masses, considering time-varying geographical boundaries, is relatively similar to the one used by Longhurst, and some of the surface water masses compare well with Longhurst (2010) biogeochemical provinces. He identified 3 provinces in the Northwestern tropical Atlantic, The North Atlantic Tropical Gyre province (NATR), the Western Tropical Atlantic province (WTRA) and the Guianas Coastal province. The NATR province is defined as the region north of the North Equatorial Current (12°N-14°N) and east of the lesser Antilles. NATR consistently has the lowest surface Chl*a* of the North Atlantic. The North Atlantic Subtropical Waters of this paper represent the same physical and biogeochemical processes as NATR and we found differences in reference to the WTRA and GUIA provinces. WTRA includes geographically the NBC and modified NBC waters. However, while the retroflection of the NBC is mentioned in the physical characteristics of the WTRA, the eddies are also mentioned in the GUIA province. The GUIA province includes all coastal processes, in this case it can be the freshwater plume, as well as high CO_2 coastal waters, and the NBC rings to a certain extent. The latter emphasizes the need to take into account the finer scale in highly dynamic regions.

4.2 Integrated CO_2 air-sea flux

The northwestern tropical Atlantic present a strong seasonal variability of CO_2 air-sea fluxes (Landschützer et al., 2016). In February, waters are the coldest, and the region is a strong CO_2 sink of -1.7 TgC month⁻¹ (Figure 10). This region, located at tropical latitudes but combining characteristics of subtropical waters and river outflow, is difficult to represent in large scale climatologies. Indeed, the sink for the month of February is smaller by a factor 10 in Landschützer et al. (2020), and is also severely underestimated in Takahashi et al., (2009), but the low spatial resolution of this last product doesn't allow for a good quantitative comparison. This region has been rarely observed, and the interannual variability described in Landschützer et al., (2020)'s climatology is therefore rather uncertain. The compensating effect of different years cannot explain entirely the difference of signal observed in February 2020 with respect to the two climatologies.

Three water masses mainly contribute to the air-sea CO_2 flux, the NASW, the fresh plume and the NBC retroflection. The NASW contributes to about 60% of the total sink and are not well captured in climatologies, with noticeable differences of

more than 20 µatm between the measured ΔfCO_2 in 2020 and the one computed from Landschützer et al., (2020) and Takahashi et al., (2009) (the closest grid point is considered for this comparison). The retroflection is the main region with a positive air-sea CO_2 flux. Its influence is observed up to 10°N-55°W, but its area is small so its impact on the regional flux is weak. The

485   positive flux of the retroflection is slightly overestimated in the climatologies, but it could also be due to the difficulty to detect the retroflection at the beginning of February. The main difference is that the NBC waters rich in CO_2 are localized in the retroflection area, and are heavily modified when spreading into the Eddy Boulevard.

The freshwater plume is a feature previously not well described for this region in winter and we found a contribution of almost 20 % to the sink. The impact of the Amazon River has been overlooked so far in winter, but it accounts for a large part of the

490   salinity and biogeochemical variability. Freshwater from the Amazon is not just located on the shelf, but it can spread northward advected by the strong currents variability associated to the NBC rings (Reverdin et al., 2021). These rings are the largest, faster rotating and are the most energetic during boreal winter compared to other seasons (Aroucha et al., 2020). Combined with a seasonal increase in the Amazon's outflow, it induces a large variability in SSS, Chl*a* and fCO_2. The occurrence of freshwater export from the shelf to the open ocean has a strong influence on the salinity and therefore on the

495   mixed layer depth and air-sea heat exchanges (Reverdin et al., 2021). It also strongly impacts the biogeochemistry of the region as the low fCO_2 is both due to the low salinity of the plume waters and to the biological activity. The plume stirred into the open ocean by the NBC rings brings nutrients in a region strongly nutrient-limited, and generates a local winter bloom. This in turns plays an important role on the air-sea CO_2 flux, and is a crucial feature of the southern part of the northwestern tropical Atlantic.

500   **4.3 Extension to other years and interannual variability**

Few tropical Atlantic measurements of biogeochemical tracers are available, in particular in the northwestern tropical Atlantic. The EUREC[4]A-OA/ATOMIC campaign provides the first in-situ comprehensive measurements of fCO_2 in this region for the boreal winter season. The reconstruction of fCO_2 maps likely provides a good understanding of the spatial evolution of fCO_2 and air-sea CO_2 fluxes, and is fitted for the months of January-February 2020. Although the processes described here are

505   specific to winter and thus cannot be extended to other seasons, they will be useful to understand the winter variability of other years.

 Only a few cruises cross the region according to the SOCAT database between 2010 and 2019 (period with satellite SSS data) and investigating inter-annual variability is not possible. However, we can test the relation developed for 2020 for other years by using select cruises from the SOCAT database. We thus first use the relationship to reconstruct fCO_2 along the ship tracks

510   (using in-situ SSS and SST and colocalized Chl*a*) and then over the whole region based on satellite products (OSTIA SST, Globcolour Chl*a*, SSS+CCI, detailed in the appendix A). A comparison between the measured and reconstructed fCO_2 for the water masses sampled by the SOCAT cruises (NASW, fresh plume, NBC retroflection, modified NBC) is presented in the appendix (Table A1). Good agreement is found between the fCO_2 from the SOCAT database and the one reconstructed from the in-situ temperature and salinity, and colocalized Chl*a* for the four water masses (averaged difference of 5.5 µatm). When

515   comparing reconstructed fCO₂ maps with fCO₂ on ship tracks (Figure A1), the agreement between fCO₂ in various water

masses is very clear, even though the spatial structures are sometimes a bit misplaced. This is attributable to the slightly coarser

resolution of satellite products not designed specifically for each campaign, to the high spatio-temporal variability of fCO₂ and

to missing Chl*a* and SST observations in cloudy areas. February 2020 was mainly cloud free, so that we were able to use high

resolution daily SST and Chl*a*. The SSS product used in 2020 is also a daily product. However, for the other years, the satellite

520   CCI Chl*a* (if clouds) and SSS products have a weekly temporal resolution, which smear the fast-moving structures. The

gradients between water masses are therefore not always well represented, but we find a good agreement between the fCO₂ of

each structure, which is encouraging for future studies on interannual variability in winter.

        By identifying the main processes responsible for the variability of the air-sea CO₂ flux in 2020, we can better understand the

525   interannual variability of the region. Indeed, each of the main water mass has its own interannual variability that shapes the

CO₂ variability. The northern part of the domain is dominated by the variation of temperature, and therefore its interannual

variability is linked to the one of SST. From 32 years monthly mean SST data, the SST standard deviation in the area is

relatively weak, and doesn't exceed 0.5°C. The northern sink of CO₂ is therefore rather similar from year to year, coherent

with the low standard deviation of the air-sea CO₂ flux computed from Landschützer et al., (2020).

530   As previously stated, most of the variability occurs south of Barbados. The freshwater plume sampled during EUREC⁴A-OA

is a common feature in February. During the 2010-2019 period, events of freshwater reaching the open ocean were observed

each year, and freshwater plumes similar to the one described in this paper were observed during 7 out of 10 years from satellite

salinity data (Reverdin et al., 2021). Two of the main mechanisms driving the occurrence of the plume are the winds near the

Amazon estuary that can induce along shelf transport to the Guyana plateau and the presence of NBC rings. This region is

535   commonly crossed by several NBC rings during winter (Jochumsen et al., 2010; Johns et al., 2003; Mélice & Arnault, 2017)

but it also is subject to a strong year to year variability that has linkages with the variability of the Amazon River outflow

(Aroucha et al., 2020). Therefore, identifying and understanding the processes happening in 2020 should contribute to better

assess the interannual variability of fCO₂ as well as air-sea CO₂ fluxes in the northwestern tropical Atlantic during winter.

Using a combination of SSS, SST and Chl*a* brings information on the biogeochemistry of the area in winter and represent well

540   the mesoscale structure.

5. Conclusion

The EUREC⁴A-OA/ATOMIC campaign provides for the first time synoptic measurements related to the air-sea fluxes of CO₂

in the northwestern tropical Atlantic in winter. Six main surface water masses are identified, one of them north of Barbados

(North Atlantic Subtropical Water), and the other five (the NBC retroflection, modified NBC waters, the freshwater plume,

545   the shelf water and the shelf filament) south of Barbados. The investigation highlights the two different regimes of the region.

In the northern part, the variability of the CO₂ flux is low and the area is covered by relatively cold, saline and low-chlorophyll

NASW. The southern part is highly variable, due to the presence of large mesoscale anticyclonic eddies. In January and February 2020, two NBC rings influence the physical and biogeochemical properties of the region. The NBC retroflection is characterized by waters with equatorial origins that are relatively warm, saline and high in fCO_2. As the rings separate from

550   the retroflection, they interact with the surrounding waters, and the initial signal in fCO_2 is dampened. The main impact of the rings is therefore not necessarily on the surface water they transport in their core, but rather on the filament they stir off the coast. A fresh plume from the Amazon River is transported by the coastal current up to the French Guiana shelf in the beginning of February. The NBC rings entrain the plume of freshwater up to 12°N. This plume is fresh, rich in Chl$a$ and low in fCO_2 and strongly contrasts with the surrounding waters and spreads over ~100 000 km^2. On the shelf not influenced by the plume water

555   is relatively saline, high in fCO_2 and Chl$a$, probably due to high concentration of detrital material. As ring A2 propagates westward, it continuously stirs a thin (10 km wide) filament of high fCO_2 shelf water up to 12°N.

Based on the ship observations we identify distinct regime in fCO_2 linked to certain combinations of SST, SSS, and Chl$a$ properties. We use this information to construct high-resolution maps of fCO_2 and air-sea CO_2 flux using satellite maps of

560   SSS, SST and Chl$a$. On average over the month of February, the region acts as a strong sink of CO_2 (-1.7 TgC/month), the sink being five times smaller in air-sea CO_2 flux climatologies. The NASW contributes for most of the flux (60%) due to low temperature associated to winter cooling and strong winds. South of Barbados, the region acts also as a sink of CO_2. The influence of equatorial water is localized to the retroflection region that acts as a small source of CO_2. The main feature in this part of the domain is the fresh plume that contributes to almost 20% of the total sink.

565   The processes described here highlight the high variability of air-sea CO_2 fluxes in winter, that are quite different from the ones in summer. These features are relatively common in winter and can be used to better understand the interannual variability of air-sea CO_2 fluxes. The northern part of the domain is driven by the variability in SST, while the southern one is a combination of the interannual variability of temperature, salinity and chlorophyll. It is therefore linked to the year-to-year variability of the NBC rings and the Amazon outflow.

570   This study is limited by the paucity of data in the region and for this time period. More fCO_2 data closer to the coast would help to better quantify the influence of shelf water on the flux. The signature of the NBC rings has been described for only two rings that had different signatures. In order to reach more robust conclusions on the transport of surface NBC water by the rings, more eddies should be observed. The variability of fCO_2 occurs at large and small scale. Salinity is one of the most valuable predictors of fCO_2 south of 10°N, but the satellite salinity resolution is much lower than the one of temperature and

575   chlorophyll. To have a more accurate prediction of the fCO_2, a high-resolution SSS product would also be very useful.

Appendix A

Due their long time series, the following SST, Chl*a* and SSS products are used to reconstruct fCO₂ maps in winter in the northwestern tropical Atlantic for other years than 2020. Results are shown on Figure A1. They are different than the satellite products used in the main study, that were only available on a short period.

580   The Operational Sea Surface Temperature and Sea Ice Analysis (OSTIA) SST product, distributed by the CMEMS is used here. Daily maps of SST are produced at a resolution of 1/20°, available from 1981 to present. OSTIA SST uses most SST data available for a day, from both infrared and microwave inferred SST.

Surface Chl*a* from GlobColour dataset derived from ocean color at a 1/24° resolution is used. It is a merged product from multiple satellite missions' observations (SeaWiFS, MERIS, MODIS, VIIRS NPP, OLCI-A, VIIRS JPSS-1 and OLCI-B).

585   GlobColour data is developed, validated, and distributed by ACRI-st.

We also use SMOS and SMAP combined weekly SSS generated by the Climate Change Initiative Sea Surface Salinity (CCI + SSS) project (https://doi.org/10.5285/4ce685bff631459f- b2a30faa699f3fc5). It provides weekly level-3 SSS data from 2010 to 2019 at a spatial resolution of 50 km, a sampled on a 25 km x 25 km grid, and 1 day, by combining data from the SMOS, Aquarius, and SMAP missions.
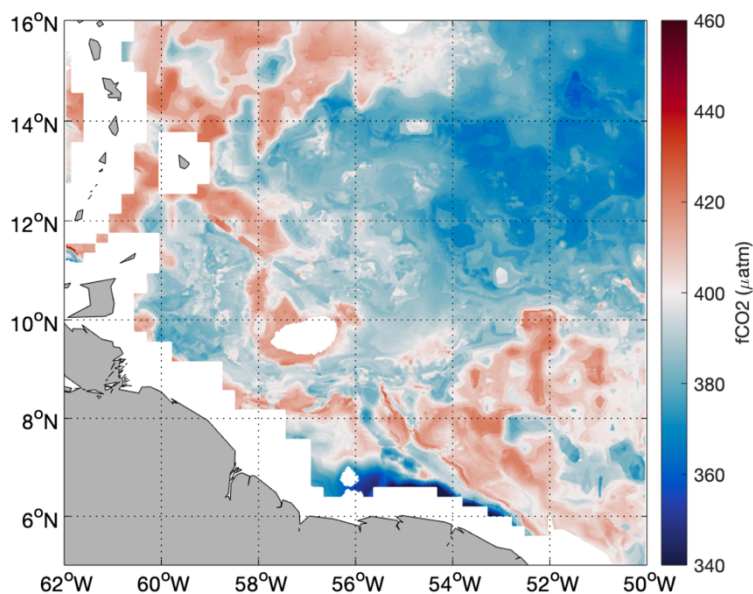
590

Figure A1. fCO₂ reconstructed from OSTIA SST, CCI+SSS and Globcolour Chl*a* for the 23/12/2015 superimposed with the fCO₂ from cruise 642B20151209.

595

	Fresh plume	**NBC waters**	**Modified NBC**	**NASW**
SOCAT fCO$_2$	316.2	413.4	385.8	349
fCO$_2$ reconstructed from SOCAT SST & SSS	310.7	410.7	392.9	358.7
Transect date	2016/01/05	2016/01/08	2015/12/23	2013/02/10
Ship Name	Colibri (France)	Colibri (France)	MSC Marianna (Panama)	Benguela Stream (Netherlands)
Expocode	35MJ20151229	35MJ20160107	642B20151209	33RO20130108

Table A1. Comparison for the 4 main water masses between the fCO$_2$ from SOCAT transect and the fCO$_2$ reconstructed from in-situ SSS and SST and colocalized Chl*a*.

600 **Code Availability**

Code used in this study can be made available upon reasonable request to the corresponding author.

Data Availability

We benefited from numerous data sets made freely available and listed here: the ADT produced by Ssalto/Duacs distributed by CMEMS (https://resources.marine.copernicus.eu), the Chl*a* and SST maps produced by CLS
605 (**https://datastore.cls.fr/catalogues/chlorophyll-high-resolution-daily** and **https://datastore.cls.fr/catalogues/sea-surface-temperature-infra-red-high-resolution-daily**), the SMOS L2Q field produced by CATDS (CATDS, 2019) (https://10.12770/12dba510-cd71-4d4f-9fc1-9cc027d128b0), the SMAP maps produced by Remote Sensing System (RSS v4 40 km), the CCI+SSS maps produced in the frame of ESA CCI+SSS project (**https://10.5285/4ce685bff631459fb2a-30faa699f3fc5**), the OSTIA SST and Copernicus -GlobColour Chl*a* distributed by the CMEMS
610 (SST_GLO_SST_L4_REP_OBSERVATIONS_010_011 and OCEANCOLOUR_GLO_CHL_L4_REP_OBSERVATIONS_009_082).
The RV Atalante fCO$_2$ is available on the SEANOE website: doi/10.17882/83578. The RV Ron Brown and RV Merian fCO$_2$ data can be found on the SOCAT database (expocodes 33RO20200106 and 06M220200117 respectively). The Surface Ocean

CO$_2$ Atlas (SOCAT) is an international effort, endorsed by the International Ocean Carbon Coordination Project (IOCCP), the

615   Surface Ocean Lower Atmosphere Study (SOLAS) and the Integrated Marine Biosphere Research program, to deliver a uniformly quality-controlled surface ocean CO$_2$ database. The many researchers and funding agencies responsible for the collection of data and quality control are thanked for their contributions to SOCAT.

Author contribution

620   LO, JB, GR and NL conceptualized the project. LO carried out the measurements and data analysis. LO, JB, GR, NL and PL contributed to result interpretation. PL, MR and RW provided the crucial datasets. LO, MR, SS and JK conducted field work. LO wrote the manuscript with input from all co-authors.

Competing interests

Some authors are members of the editorial board of Biogeosciences. The peer-review process was guided by an independent

625   editor, and the authors have also no other competing interests to declare.

References

640   Aller, R. C., & Blair, N. E. (2006). Carbon remineralization in the Amazon–Guianas tropical mobile mudbelt: A sedimentary incinerator. *Continental Shelf Research*, *26*(17), 2241–2259. https://doi.org/10.1016/j.csr.2006.07.016

Andrié, C., Oudot, C., Genthon, C., & Merlivat, L. (1986). CO2 fluxes in the tropical Atlantic during FOCAL cruises. *Journal of Geophysical Research: Oceans*, *91*(C10), 11741–11755. https://doi.org/10.1029/JC091iC10p11741

Aroucha, L. C., Veleda, D., Lopes, F. S., Tyaquiçã, P., Lefèvre, N., & Araujo, M. (2020). Intra- and Inter-Annual Variability
645 of North Brazil Current Rings Using Angular Momentum Eddy Detection and Tracking Algorithm: Observations From 1993 to 2016. *Journal of Geophysical Research: Oceans*, *125*(12), e2019JC015921. https://doi.org/10.1029/2019JC015921

Arrigo, K. R. (2007). Marine manipulations. *Nature*, *450*(7169), 491–492. https://doi.org/10.1038/450491a

Arruda, R., Atamanchuk, D., Cronin, M., Steinhoff, T., & Wallace, D. W. R. (2020). At-sea intercomparison of three underway pCO2 systems. *Limnology and Oceanography: Methods*, *18*(2), 63–76. https://doi.org/10.1002/lom3.10346

650 Bakker, D. C. E., Pfeil, B., Landa, C. S., Metzl, N., O'Brien, K. M., Olsen, A., et al. (2016). A multi-decade record of high-quality fCO$_2$ data in version 3 of the Surface Ocean CO$_2$ Atlas (SOCAT). *Earth System Science Data*, *8*(2), 383–413. https://doi.org/10.5194/essd-8-383-2016

Behrenfeld, M. J., O'Malley, R. T., Siegel, D. A., McClain, C. R., Sarmiento, J. L., Feldman, G. C., et al. (2006). Climate-driven trends in contemporary ocean productivity. *Nature*, *444*(7120), 752–755. https://doi.org/10.1038/nature05317

655 Chen, C.-T. A., Huang, T.-H., Fu, Y.-H., Bai, Y., & He, X. (2012). Strong sources of CO2 in upper estuaries become sinks of CO2 in large river plumes. *Current Opinion in Environmental Sustainability*, *4*(2), 179–185. https://doi.org/10.1016/j.cosust.2012.02.003

Coles, V. J., Brooks, M. T., Hopkins, J., Stukel, M. R., Yager, P. L., & Hood, R. R. (2013). The pathways and properties of the Amazon River Plume in the tropical North Atlantic Ocean. *Journal of Geophysical Research: Oceans*, *118*(12), 6894–
660 6913. https://doi.org/10.1002/2013JC008981

Dai, A., & Trenberth, K. E. (2002). Estimates of Freshwater Discharge from Continents: Latitudinal and Seasonal Variations. *Journal of Hydrometeorology*, *3*(6), 660–687. https://doi.org/10.1175/1525-7541(2002)003<0660:EOFDFC>2.0.CO;2

Entekhabi, D., Njoku, E. G., O'Neill, P. E., Kellogg, K. H., Crow, W. T., Edelstein, W. N., et al. (2010). The soil moisture active passive (SMAP) mission. *Proceedings of the IEEE*, *98*(5), 704–716.

665 Fay, A. R., & McKinley, G. A. (2014). Global open-ocean biomes: mean and temporal variability. *Earth System Science Data*, *6*(2), 273–284. https://doi.org/10.5194/essd-6-273-2014

Ffield, A. (2005). North Brazil current rings viewed by TRMM Microwave Imager SST and the influence of the Amazon Plume. *Deep Sea Research Part I: Oceanographic Research Papers*, *52*(1), 137–160. https://doi.org/10.1016/j.dsr.2004.05.013

670 Field, C. B., Behrenfeld, M. J., Randerson, J. T., & Falkowski, P. (1998). Primary Production of the Biosphere: Integrating Terrestrial and Oceanic Components. *Science*, *281*(5374), 237–240. https://doi.org/10.1126/science.281.5374.237

Font, J., Camps, A., Borges, A., Martín-Neira, M., Boutin, J., Reul, N., et al. (2009). SMOS: The challenging sea surface salinity measurement from space. *Proceedings of the IEEE*, *98*(5), 649–665.

Fournier, S., Chapron, B., Salisbury, J., Vandemark, D., & Reul, N. (2015). Comparison of spaceborne measurements of sea
675   surface salinity and colored detrital matter in the Amazon plume. *Journal of Geophysical Research: Oceans*, *120*(5), 3177–
3192. https://doi.org/10.1002/2014JC010109

Fratantoni, D. M., & Glickson, D. A. (2002). North Brazil Current Ring Generation and Evolution Observed with SeaWiFS.
Journal   of   Physical   Oceanography,   *32*(3),   1058–1074.   https://doi.org/10.1175/1520-
0485(2002)032<1058:NBCRGA>2.0.CO;2

680   Fratantoni, D. M., & Richardson, P. L. (2006). The Evolution and Demise of North Brazil Current Rings. *Journal of Physical
Oceanography*, *36*(7), 1241–1264. https://doi.org/10.1175/JPO2907.1

Friedlingstein, P., O'Sullivan, M., Jones, M. W., Andrew, R. M., Hauck, J., Olsen, A., et al. (2020). Global Carbon Budget
2020. *Earth System Science Data*, *12*(4), 3269–3340. https://doi.org/10.5194/essd-12-3269-2020

Garraffo, Z. D., Johns, W. E., P.Chassignet, E., & Goni, G. J. (2003). North Brazil Current rings and transport of southern
685   waters in a high resolution numerical simulation of the North Atlantic. In G. J. Goni & P. Malanotte-Rizzoli (Eds.), *Elsevier
Oceanography Series* (Vol. 68, pp. 375–409). Elsevier. https://doi.org/10.1016/S0422-9894(03)80155-1

Grodsky, S. A., Vandemark, D., & Feng, H. (2018). Assessing Coastal SMAP Surface Salinity Accuracy and Its Application
to Monitoring Gulf of Maine Circulation Dynamics. *Remote Sensing*, *10*(8), 1232. https://doi.org/10.3390/rs10081232

Ibánhez, J. S. P., Araujo, M., & Lefèvre, N. (2016). The overlooked tropical oceanic CO2 sink. *Geophysical Research Letters*,
690   *43*(8), 3804–3812. https://doi.org/10.1002/2016GL068020

IOCCG. (2009). *Partition of the Ocean Into Ecological Provinces: Role of Ocean-colour Radiometry*. Dartmouth Canada.

IPCC, 2019: IPCC Special Report on the Ocean and Cryosphere in a Changing Climate [H.-O. Pörtner, D.C. Roberts, V.
Masson-Delmotte, P. Zhai, M. Tignor, E. Poloczanska, K. Mintenbeck, A. Alegría, M. Nicolai, A. Okem, J. Petzold, B. Rama,
N.M. Weyer (eds.)]. In press.

695   IPCC, 2021: Climate Change 2021: The Physical Science Basis. Contribution of Working Group I to the Sixth Assessment
Report of the Intergovernmental Panel on Climate Change [Masson-Delmotte, V., P. Zhai, A. Pirani, S.L. Connors, C. Péan,
S. Berger, N. Caud, Y. Chen, L. Goldfarb, M.I. Gomis, M. Huang, K. Leitzell, E. Lonnoy, J.B.R. Matthews, T.K. Maycock,
T. Waterfield, O. Yelekçi, R. Yu, and B. Zhou (eds.)]. Cambridge University Press. In Press.

Jochumsen, K., Rhein, M., Hüttl-Kabus, S., & Böning, C. W. (2010). On the propagation and decay of North Brazil Current
700   rings. *Journal of Geophysical Research: Oceans*, *115*(C10). https://doi.org/10.1029/2009JC006042

Johns, W. E., Lee, T. N., Schott, F. A., Zantopp, R. J., & Evans, R. H. (1990). The North Brazil Current retroflection: Seasonal
structure   and   eddy   variability.   *Journal   of   Geophysical   Research: Oceans*,   *95*(C12),   22103–22120.
https://doi.org/10.1029/JC095iC12p22103

Johns, W. E., Zantopp, R. J., & Goni, Gustavo. J. (2003). Cross-gyre transport by North Brazil Current rings. In G. J. Goni &
705   P. Malanotte-Rizzoli (Eds.), *Elsevier Oceanography Series* (Vol. 68, pp. 411–441). Elsevier. https://doi.org/10.1016/S0422-
9894(03)80156-3

Karstensen, J., Lavik, G., Acquistapace, C., Bagheri, G., Begler, C., Bendinger, A., et al. (2020). *EUREC4A Campaign, Cruise No. MSM89, 17. January - 20. February 2020, Bridgetown (Barbados) - Bridgetown (Barbados), The ocean mesoscale component in the EUREC4A field study* (MARIA S. MERIAN-Berichte) (pp. 1–70). Bonn: Gutachterpanel

710   Forschungsschiffe. https://doi.org/10.2312/cr_msm89

Kerr, Y. H., Waldteufel, P., Wigneron, J.-P., Delwart, S., Cabot, F., Boutin, J., et al. (2010). The SMOS mission: New tool for monitoring key elements ofthe global water cycle. *Proceedings of the IEEE*, *98*(5), 666–687.

Körtzinger, A. (2003). A significant CO2 sink in the tropical Atlantic Ocean associated with the Amazon River plume. *Geophysical Research Letters*, *30*(24). https://doi.org/10.1029/2003GL018841

715   Landschützer, P., Gruber, N., Bakker, D. C. E., Schuster, U., Nakaoka, S., Payne, M. R., et al. (2013). A neural network-based estimate of the seasonal to inter-annual variability of the Atlantic Ocean carbon sink. *Biogeosciences*, *10*(11), 7793–7815. https://doi.org/10.5194/bg-10-7793-2013

Landschützer, P., Gruber, N., Bakker, D. C. E., & Schuster, U. (2014). Recent variability of the global ocean carbon sink. *Global Biogeochemical Cycles*, *28*(9), 927–949. https://doi.org/10.1002/2014GB004853

720   Landschützer, Peter, Gruber, N., & Bakker, D. C. E. (2016). Decadal variations and trends of the global ocean carbon sink. *Global Biogeochemical Cycles*, *30*(10), 1396–1417. https://doi.org/10.1002/2015GB005359

Landschützer, Peter, Laruelle, G. G., Roobaert, A., & Regnier, P. (2020). A uniform pCO_2 climatology combining open and coastal oceans. *Earth System Science Data*, *12*(4), 2537–2553. https://doi.org/10.5194/essd-12-2537-2020

Laxenaire, R., Speich, S., Blanke, B., Chaigneau, A., Pegliasco, C., & Stegner, A. (2018). Anticyclonic Eddies Connecting the

725   Western Boundaries of Indian and Atlantic Oceans. *Journal of Geophysical Research: Oceans*, *123*(11), 7651–7677. https://doi.org/10.1029/2018JC014270

Lefévre, N., Diverrés, D., & Gallois, F. (2010). Origin of CO2 undersaturation in the western tropical Atlantic. *Tellus B: Chemical and Physical Meteorology*, *62*(5), 595–607. https://doi.org/10.1111/j.1600-0889.2010.00475.x

Longhurst, A., Sathyendranath, S., Platt, T., & Caverhill, C. (1995). An estimate of global primary production in the ocean

730   from satellite radiometer data. *Journal of Plankton Research*, *17*(6), 1245–1271. https://doi.org/10.1093/plankt/17.6.1245

Longhurst, A. R. (2010). *Ecological Geography of the Sea*. Elsevier.

Medeiros, P. M., Seidel, M., Ward, N. D., Carpenter, E. J., Gomes, H. R., Niggemann, J., et al. (2015). Fate of the Amazon River dissolved organic matter in the tropical Atlantic Ocean. *Global Biogeochemical Cycles*, *29*(5), 677–690. https://doi.org/10.1002/2015GB005115

735   Mélice, J.-L., & Arnault, S. (2017). Investigation of the Intra-Annual Variability of the North Equatorial Countercurrent/North Brazil Current Eddies and of the Instability Waves of the North Tropical Atlantic Ocean Using Satellite Altimetry and Empirical Mode Decomposition. *Journal of Atmospheric and Oceanic Technology*, *34*(10), 2295–2310. https://doi.org/10.1175/JTECH-D-17-0032.1

Mu, L., Gomes, H. do R., Burns, S. M., Goes, J. I., Coles, V. J., Rezende, C. E., et al. (2021). Temporal Variability of Air-Sea
740   CO_2 flux in the Western Tropical North Atlantic Influenced by the Amazon River Plume. *Global Biogeochemical Cycles*,
       35(6), e2020GB006798. https://doi.org/10.1029/2020GB006798

Muller-Karger, F. E., McClain, C. R., & Richardson, P. L. (1988). The dispersal of the Amazon's water. *Nature*, *333*(6168),
       56–59. https://doi.org/10.1038/333056a0

Olivier Léa, Labaste Matthieu, Noisel Christophe, Lefevre Nathalie (2020). Underway fCO2 distribution during the
745   EUREC4A-OA experiment. SEANOE. https://doi.org/10.17882/83578

Piepmeier, J. R., Focardi, P., Horgan, K. A., Knuble, J., Ehsan, N., Lucey, J., et al. (2017). SMAP L-band microwave
       radiometer: Instrument design and first year on orbit. *IEEE Transactions on Geoscience and Remote Sensing*, *55*(4), 1954–
       1966.

Pierrot, D., Neill, C., Sullivan, K., Castle, R., Wanninkhof, R., Lüger, H., et al. (2009). Recommendations for autonomous
750   underway pCO2 measuring systems and data-reduction routines. *Deep Sea Research Part II: Topical Studies in Oceanography*,
       56(8), 512–522. https://doi.org/10.1016/j.dsr2.2008.12.005

Platt, T., Caverhill, C., & Sathyendranath, S. (1991). Basin-scale estimates of oceanic primary production by remote sensing:
       The North Atlantic. *Journal of Geophysical Research: Oceans*, *96*(C8), 15147–15159. https://doi.org/10.1029/91JC01118

Poisson, A., Metzl, N., Brunet, C., Schauer, B., Bres, B., Ruiz-Pino, D., & Louanchi, F. (1993). Variability of sources and
755   sinks of CO2 in the western Indian and southern oceans during the year 1991. *Journal of Geophysical Research: Oceans*,
       98(C12), 22759–22778. https://doi.org/10.1029/93JC02501

Quinn, P. K., Thompson, E. J., Coffman, D. J., Baidar, S., Bariteau, L., Bates, T. S., et al. (2021). Measurements from the RV
       Ronald H. Brown and related platforms as part of the Atlantic Tradewind Ocean-Atmosphere Mesoscale Interaction Campaign
       (ATOMIC). *Earth System Science Data*, *13*(4), 1759–1790. https://doi.org/10.5194/essd-13-1759-2021

760   Reverdin, G., Olivier, L., Foltz, G. R., Speich, S., Karstensen, J., Horstmann, J., et al. (2021). Formation and Evolution of a
       Freshwater Plume in the Northwestern Tropical Atlantic in February 2020. *Journal of Geophysical Research: Oceans*, *126*(4),
       e2020JC016981. https://doi.org/10.1029/2020JC016981

Richardson, P. L., Hufford, G. E., Limeburner, R., & Brown, W. S. (1994). North Brazil Current retroflection eddies. *Journal
       of Geophysical Research: Oceans*, *99*(C3), 5081–5093. https://doi.org/10.1029/93JC03486

765   Schott, F. A., Fischer, J., & Stramma, L. (1998). Transports and Pathways of the Upper-Layer Circulation in the Western
       Tropical   Atlantic.   *Journal   of   Physical   Oceanography*,   *28*(10),   1904–1928.   https://doi.org/10.1175/1520-
       0485(1998)028<1904:TAPOTU>2.0.CO;2

Speich Sabrina, The Embarked Science Team (2021). EUREC4A-OA. Cruise Report. 19 January – 19 February 2020. Vessel
       : L'ATALANTE. https://doi.org/10.13155/80129

770   Stevens, B., Bony, S., Farrell, D., Ament, F., Blyth, A., Fairall, C., et al. (2021). EUREC[4]A. *Earth System Science Data*, *13*(8),
       4067–4119. https://doi.org/10.5194/essd-13-4067-2021

Stum, J., Tebri, H., Lehodey, P., Senina, I., Greiner, E., & Lucas, M. (n.d.). NRT operational chlorophyll maps calculation for marine applications, 1.

Subramaniam, A., Yager, P. L., Carpenter, E. J., Mahaffey, C., Björkman, K., Cooley, S., et al. (2008). Amazon River enhances

775   diazotrophy and carbon sequestration in the tropical North Atlantic Ocean. *Proceedings of the National Academy of Sciences*, *105*(30), 10460–10465. https://doi.org/10.1073/pnas.0710279105

Takahashi, T., Sutherland, S. C., Sweeney, C., Poisson, A., Metzl, N., Tilbrook, B., et al. (2002). Global sea–air CO2 flux based on climatological surface ocean pCO2, and seasonal biological and temperature effects. *Deep Sea Research Part II: Topical Studies in Oceanography*, *49*(9), 1601–1622. https://doi.org/10.1016/S0967-0645(02)00003-6

780   Takahashi, T., Sutherland, S. C., Wanninkhof, R., Sweeney, C., Feely, R. A., Chipman, D. W., et al. (2009). Climatological mean and decadal change in surface ocean pCO2, and net sea–air CO2 flux over the global oceans. *Deep Sea Research Part II: Topical Studies in Oceanography*, *56*(8), 554–577. https://doi.org/10.1016/j.dsr2.2008.12.009

Wanninkhof, R., Lewis, E., Feely, R. A., & Millero, F. J. (1999). The optimal carbonate dissociation constants for determining surface water pCO2 from alkalinity and total inorganic carbon. *Marine Chemistry*, *65*(3), 291–301.

785   https://doi.org/10.1016/S0304-4203(99)00021-3

Wanninkhof, R. (2014). Relationship between wind speed and gas exchange over the ocean revisited. *Limnology and Oceanography: Methods*, *12*(6), 351–362. https://doi.org/10.4319/lom.2014.12.351

Weiss, R. F. (1974). Carbon dioxide in water and seawater: the solubility of a non-ideal gas. *Marine Chemistry*, *2*(3), 203–215. https://doi.org/10.1016/0304-4203(74)90015-2

790   Wilson, W. D., Johns, W. E., & Garzoli, S. L. (2002). Velocity structure of North Brazil Current rings. *Geophysical Research Letters*, *29*(8), 114-1-114–4. https://doi.org/10.1029/2001GL013869

795